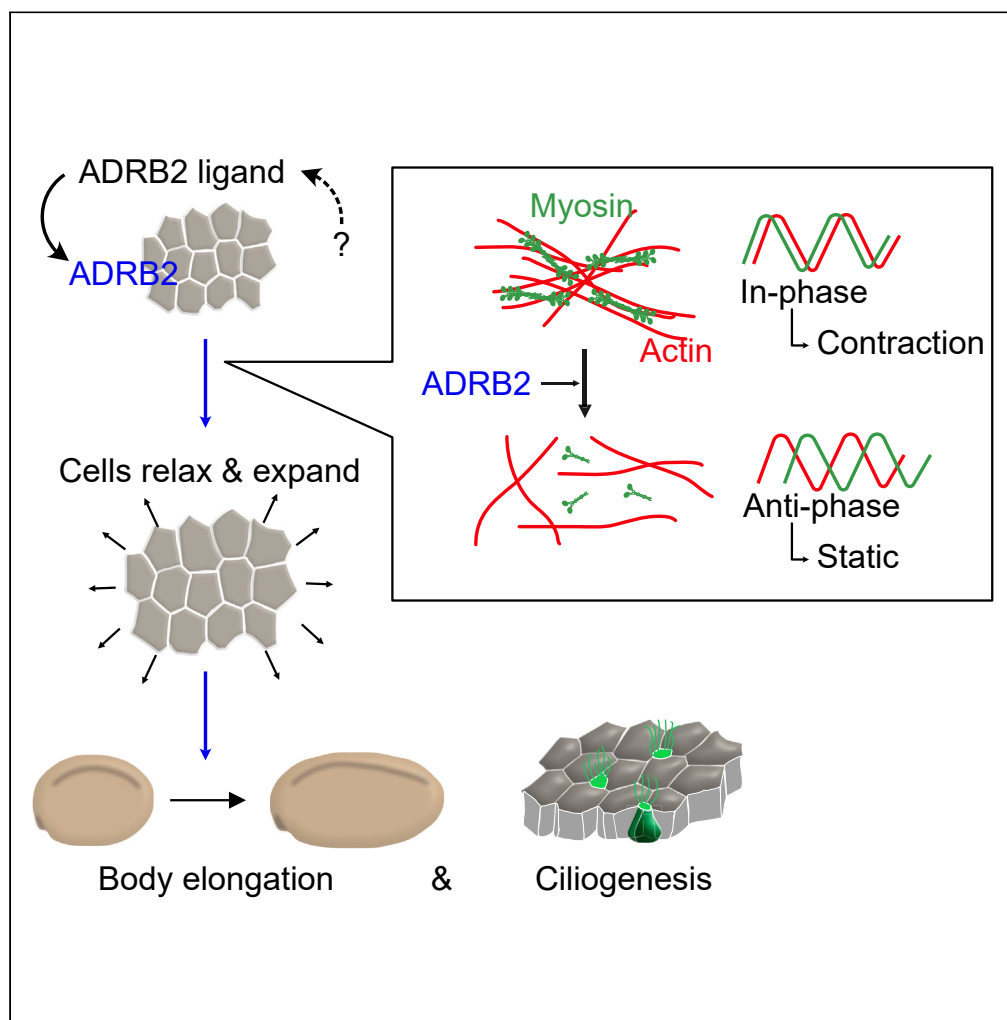# iScience

Article

β-adrenergic receptor regulates embryonic epithelial extensibility through actomyosin inhibition

Yohei Mizoguchi,
Kaoru Nakashima,
Ayato Sato, Asako
Shindo

shindo@kumamoto-u.ac.jp

Highlights

Chemical screening shows
ADRB2 suppresses
actomyosin contractility in
epidermis

ADRB2 expands the apical
cell surface in the
epidermis

ADRB2 suppresses the
synchronous oscillation of
F-actin and myosin

ADRB2 ligand is crucial for
expanding embryonic
epidermal cell surface

Article

β-adrenergic receptor regulates embryonic epithelial extensibility through actomyosin inhibition

Yohei Mizoguchi,[1] Kaoru Nakashima,[2] Ayato Sato,[3] and Asako Shindo[2,4,*]

SUMMARY

During morphogenesis, epithelial tissues reshape and expand to cover the body and organs. The molecular mechanisms of this deformability remain elusive. Here, we investigate the role of the β-adrenergic receptor (ADRB) in orchestrating actomyosin contractility, pivotal for epithelial extensibility. Chemical screens on *Xenopus laevis* embryos pinpointed ADRB2 as a principal regulator. ADRB2 promotes actomyosin relaxation, facilitating apical cell area expansion during body elongation. In contrast, ADRB2 knockdown results in heightened cell contraction, marked by synchronous oscillation of F-actin and myosin, impeding body elongation. ADRB2 mutants with reduced affinity for ligand binding lack the function to induce cellular relaxation, highlighting the ligand's essential roles even in the developing epidermis. Our findings unveil ADRB2's critical contribution to extensibility of the epidermis and subsequent body elongation during development. This study also offers insights into the physiology of mature epithelial organs deformed by the smooth muscle response to the adrenergic autonomic nervous system.

INTRODUCTION

Epithelial tissues exhibit remarkable deformability, undergoing significant morphological alteration while maintaining a cohesive sheet-like structure. During embryonic development, pronounced changes manifest in epithelium—the outermost layer—highlighting its inherent adaptability in dynamically reshaping itself.[1,2] For example, in *Drosophila* germband extension, despite the actomyosin-driven convergent extension exerting localized contractile forces, the elongating epithelium remains undamaged.[3,4] Similarly, in *Xenopus* neural tube closure, while apical constriction on the dorsal side exerts stretching forces on lateral and ventral epidermal sheets,[5,6] the epidermis retains its structural integrity. In adults, epithelial organs such as the trachea and uterus frequently experience deformation due to autonomic nervous system-regulated smooth muscle contraction and relaxation. Yet, their epithelial layer persistently stays intact, underscoring the intrinsic deformability of epithelial structures. The *in vivo* mechanisms underpinning their remarkable deformability remain unresolved in developmental biology and physiology.[7]

Elucidating the regulatory mechanisms that balance actomyosin contraction and relaxation is fundamental to understanding epithelial deformability. Actomyosin contractility plays a pivotal role during embryonic tissue morphogenesis[8,9] and is largely governed by the phosphorylation of the myosin light chain.[10] Notably, proteins such as myosin light-chain kinase (MLCK), Rho-associated protein kinase (ROCK),[11,12] and myosin light chain phosphatase (MLCP) dynamically orchestrate actomyosin contraction activities. Such regulation results in oscillations in contractility, which efficiently drives tissue morphogenesis.[13,14] While there has been significant research into the role of actomyosin in collective cell dynamics, the precise mechanisms that maintain the equilibrium between contraction and relaxation remain unclear.

In this study, we sought to identify and characterize the crucial regulators of actomyosin contractility in the epidermis using a chemical screening system established on *Xenopus* embryos, a widely used *in vivo* epithelial model. Using a US Food and Drug Administration (FDA)-approved drug library, known for its well-defined target molecules, we induced actomyosin hypercontraction in the *Xenopus* epidermis using calyculin A (CLA), a recognized phosphatase inhibitor.[15–17] CLA caused significant hypercontraction, damaging the epidermis (Figures 1A and S1A). We then combined CLA with 152 FDA-approved chemicals to discern their potential inhibitory effects on CLA-induced contractility. Our goal was to pinpoint molecular targets capable of modulating the excessive actomyosin contractility elicited by CLA. This approach offers insights into the molecules essential for controlling epidermal deformability.

In the embryonic epidermis screening, the β2-adrenergic receptor (ADRB2),[18,19] predominantly recognized for its functions in the adult autonomic nervous system, emerged as a potential regulator for actomyosin relaxation. Intriguingly, the embryos analyzed in this research had not yet formed a nervous system, suggesting a non-neuronal role of ADRB2 within the epidermis. This study elucidates the underlying mechanisms preserving epithelial integrity against mechanical distortion during development.

[1]Division of Biological Sciences, Department of Molecular Biology, Nagoya University Graduate School of Science, Nagoya 464-8602, Japan
[2]Institute of Molecular Embryology and Genetics, Kumamoto University, Kumamoto 860-0811, Japan
[3]Institute of Transformative Bio-Molecules (WPI-ITbM), Nagoya University, Nagoya 464-8601, Japan
[4]Lead contact
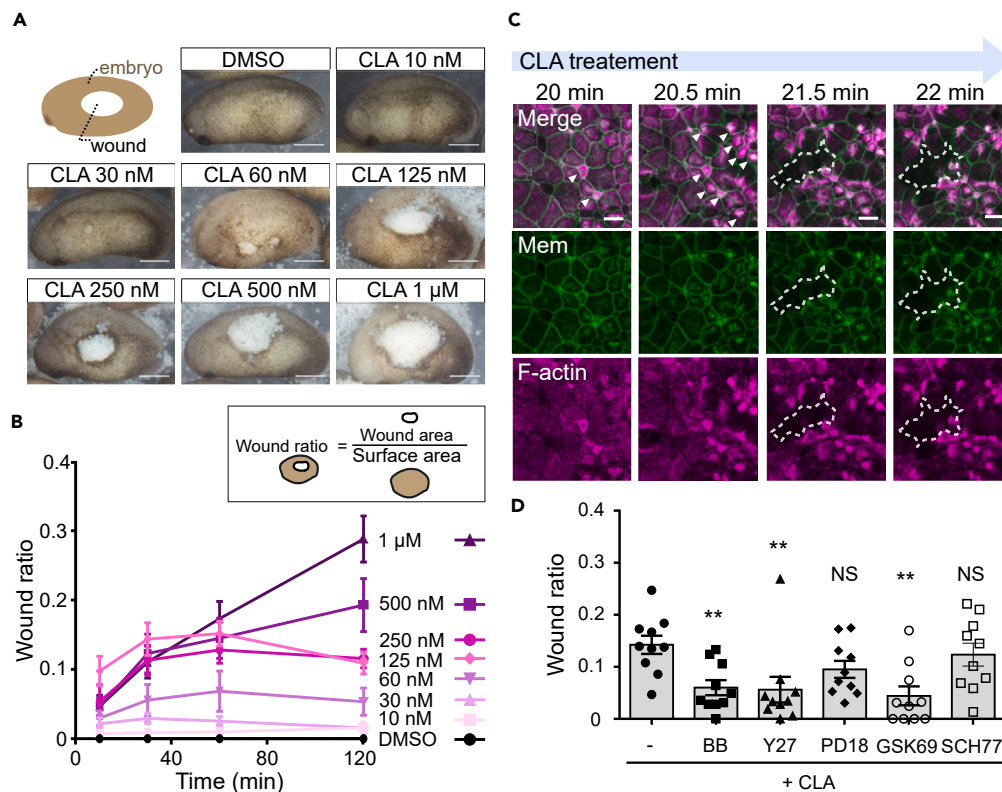*Correspondence: shindo@kumamoto-u.ac.jp

Figure 1. CLA tears the *Xenopus* embryo epidermis by eliciting hypercontraction of actomyosin

(A) Late neurula stage embryos, at 1 h after CLA treatment. The white area on the epidermis is the wound. Scale bar: 0.5 mm.

(B) Time-course analysis of the CLA-induced wound area. The wound area was divided by the embryo surface area, to quantify the effects of CLA. Data are represented as mean ± SEM.

(C) Still images from live-imaging of the epidermis, at 15–22 min after CLA treatment (1 µM). The embryos expressed LifeAct-RFP (F-actin marker) and a membrane marker. Arrowheads indicate ectopic accumulation of F-actin, while dotted lines indicate the torn area. Scale bar: 20 µm.

(D) Wound ratio at 10 min after treatment with inhibitors. Co-treatment with CLA (200 nM) and an actomyosin or kinase-related inhibitor: BB (myosin II inhibitor), 100 µM; Y27 (ROCK inhibitor), 100 µM; PD18 (ERK inhibitor), 10 µM; GSK69 (Akt kinase inhibitor), 1 µM; and SCH77 (ERK1/2 inhibitor), 1 µM. The concentrations used were about IC_{50} in cell-based assays × 100–500. Scale bar: 0.5 mm. (n = 10, **p < 0.01, as assessed using one-way analysis of variance, Data are represented as mean ± SEM). (CLA, calyculin A; ROCK, Rho-associated protein kinase; MLCK, myosin light-chain kinase; ERK, extracellular signal-regulated kinase).

RESULTS

CLA-induced actomyosin hypercontraction disrupts epidermal integrity

We developed a chemical assay for identifying regulators of actomyosin dynamics in the developing *Xenopus* epidermis (Figure 1). The primary objective of this screening was to isolate compounds capable of attenuating the pronounced contraction induced by CLA. Upon administering concentrations exceeding 60 nM of CLA to the embryos, we observed visible epidermal damage within 60 min in Stage 20 neurula embryos, characterized by the formation of circular wound (Figure 1A). The epidermal damage induced by CLA predominantly appeared at either single or multiple locations, especially in areas where cells underwent internal or external mechanical stress. These sites include the neural tube,[5] the blastopore,[20] and the interface with the culture dish. Once damage initiation occurred at a particular site, the damage progression was evident, often bridging multiple damage sites (Figure S1A).

To further our analysis, the images of the embryos were converted into a binary format, enabling the measurement of the embryo surface and wound areas. In instances where embryos exhibited multiple damage sites, the cumulative damaged area was calculated by aggregating the areas of all individual sites (Figure S1B). The ratio of the wound-to-embryo surface area revealed a dose-dependent increase in response to CLA, with a notable increase at concentrations exceeding 500 nM (Figure 1B).

To elucidate whether CLA-induced wound formation originated from enhanced actomyosin contraction, we performed live-imaging of the epidermis following CLA treatment. At 20 min post 1 µM CLA exposure, F-actin accumulated at the apical cell surface, leading to a reduction in cell surface area (Figure 1C, arrowheads). Within the subsequent minute, cell contraction perturbed the integrity of the epidermal sheet (Figure 1C, dotted line). Concurrent treatment with either Y27632 (Y27) or blebbistatin (BB), inhibitors of ROCK and myosin heavy chain ATP binding, respectively, attenuated the effects of CLA and diminished the wound ratio (Figures 1D and S1B). These findings suggest that wounds induced by CLA arise from intensified actomyosin contractility.
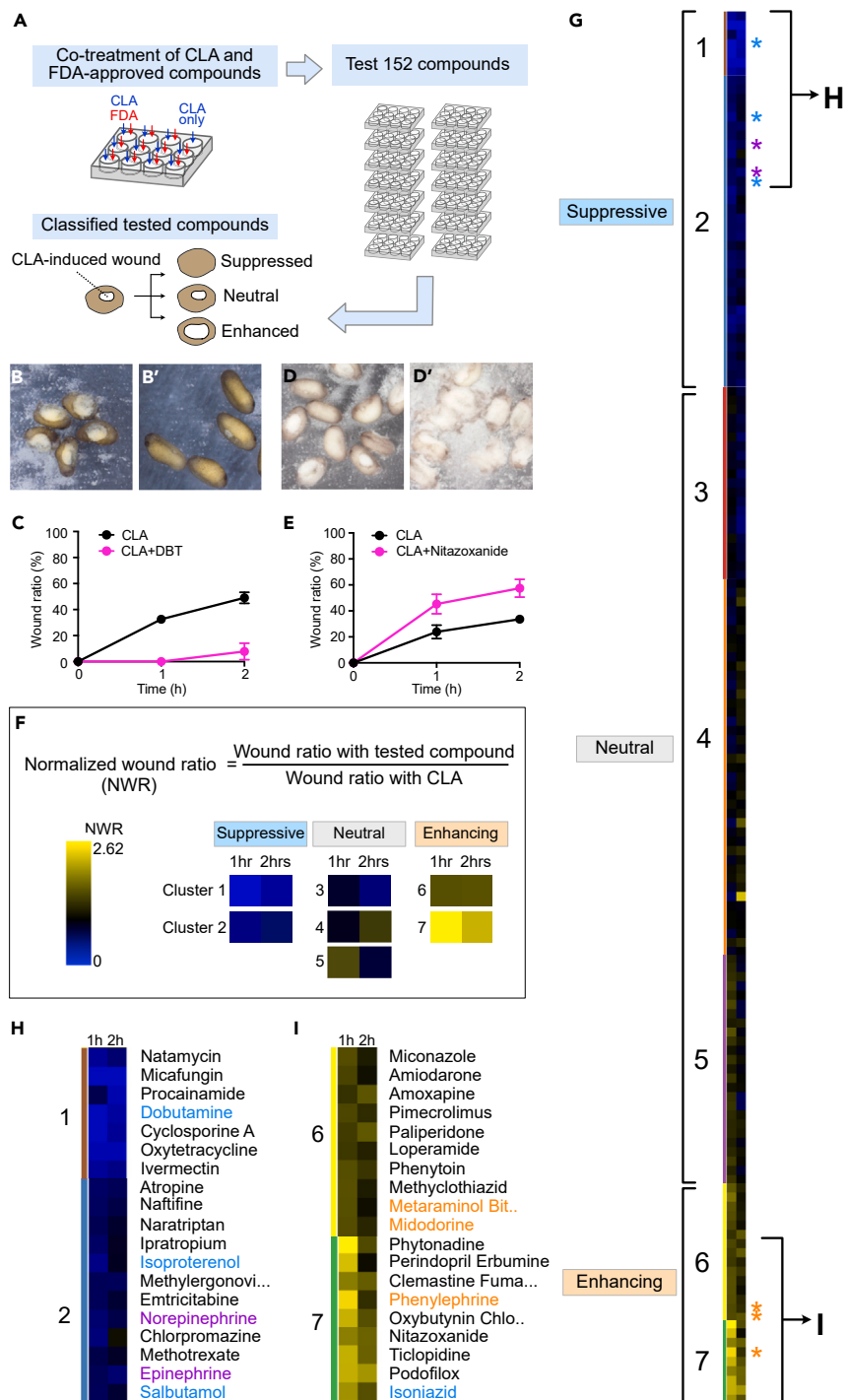
Figure 2. Chemical screening for the detection of adrenergic receptors

(A) The screening procedure. Five to ten embryos in each well were treated with CLA and FDA-approved compounds. In the study, 152 compounds were tested and the effect was classified based on the wound size.

(B and B') Example compounds classified as suppressive: CLA (B) and CLA and DBT (B').

(C) Wound ratio for embryos shown in B and B', calculated to quantify the suppressive effect of DBT against CLA.

(D and D') Example compounds classified as enhancing: CLA (D) and CLA and nitazoxanide (D').

(E) Wound ratio for embryos shown in (D) and (D').

(F) Wound ratio of each FDA-approved compound, normalized to the CLA wound ratio (NWR). NWR values at 1 and 2 h after treatment were converted to heatmap colors using Web MeV (http://mev.tm4.org/).

Figure 2. Continued

(G) Clustering of compounds based on the heatmap colors. Blue asterisks indicate ADRB agonists; purple asterisks indicate norepinephrine and epinephrine; orange asterisks indicate ADRA agonists.

(H) Zoom-in view of Cluster 1 and 2 compounds from (G).

(I) Zoom-in view of Cluster 6 and 7 compounds from (G). (Data in C and E are represented as mean ± SEM. CLA, calyculin A; FDA, US Food and Drug Association; NWR, normalized wound ratio; ADRA, alpha-adrenergic receptor; ADRB, beta-adrenergic receptor).

We explored the potential involvement of other phosphorylated proteins in wound formation. To identify potential myosin light chain (MYL) phosphorylation pathways in the epidermis, we employed CLA in conjunction with inhibitors of Akt (GSK690693), extracellular signal-regulated kinase (ERK; SCH772984), and mitogen-activated protein kinase kinase (MEK) (PD184352/CI-1040, PD18).[21] Among these, only the Akt inhibitor suppressed CLA-induced wound formation (Figures 1D and S1B), implying a possible role of Akt activation in this phenomenon. Administering these kinase inhibitors alone caused no epidermal abnormalities (Figure S1C). Taken together, these findings underscore that CLA-induced actomyosin hypercontraction results in wound formation, serving as a pertinent metric for screening compounds that target actomyosin contractility.

Compound screening reveals ADRB agonists that counteract CLA effects

We subjected an FDA-approved compound library to a screening process to identify regulators of actomyosin contractility. A subset of 152 compounds was randomly selected from this library (Table S1) and subsequently assayed on 5–10 embryos at a concentration of 10 μM in conjunction with 500 nM CLA (Figure 2A). The concentration of 500 nM CLA was chosen based on the significant wound expansion previously observed at this level (Figure 1B). The tested compounds were categorized according to their effect on CLA-induced wound formation (Figures 2B–2G). For instance, the ADRB agonist dobutamine (DBT)[22,23] strongly suppressed wound formation, displaying minimal wounds 1–2 h post-exposure (Figures 2B, 2B', and 2C). Conversely, nitazoxanide exacerbated the wound-inducing properties of CLA, leading to extensive epidermal disruption; however, potential non-specific effects of the compound should be considered (Figures 2D, 2D', and 2E).

To systematically assess the effects of the FDA-approved compounds on CLA-induced damages, we calculated the wound ratio at 1 and 2 h post-treatment and subsequently normalized this ratio against that of CLA alone, yielding the normalized wound ratio (NWR; Figure 2F and Table S2). Using the NWR values, we performed non-hierarchical clustering, which classified the compounds into seven distinct clusters (Figure 2G; Table S3). Through heatmap analysis, these clusters were delineated as either "suppressive," "neutral," or "enhancing" effects on wound formation (Figure 2F). Our focused analysis centered on Clusters 1 and 7, representing compounds with suppressive or enhancing effects on CLA-driven wound formation, respectively (Figures 2G–2I).

Cluster 1, characterized by compounds antagonizing CLA activity, comprised antibiotics, antifungal agents, antiprotozoal agents, sodium channel blockers, phosphate inhibitors, and an ADRB agonist (Figure 2H, Cluster 1). Cluster 7, which amplified CLA-induced effects, encompassed antiparasitics, antibiotics, antiviral agents, adenosine diphosphate receptor inhibitors, anticholinergics, and α1-adrenergic receptor (ADRA1) agonists (Figure 2I). Three ADRB agonists—DBT, isoproterenol, and salbutamol—were grouped within Clusters 1 and 2 as suppressive agents (Figures 2H [light blue] and S2A–S2D), with endogenous ADRB ligands, norepinephrine, and epinephrine situated in Cluster 2 (Figure 2H [purple]; Table S3). Notably, Cluster 7 had the ADRA1 agonist phenylephrine, while two other ADRB1 agonists appeared in Cluster 6 (Figure 2I [orange]; Table S3). Given the contrasting roles α1- and β-adrenergic receptors play in smooth muscle contraction,[24–26] our observations propose a potential equilibrium mediated by these receptors in actomyosin contraction and relaxation in the epidermis.

DBT suppresses CLA-induced epidermal wounding via ADRB activation

We next examined ADRB expression in the developing *Xenopus* epidermis. Previous studies employing reverse-transcription quantitative polymerase chain reaction identified the expression of *Xenopus* ADRB1 RNA (*adrb1*) in whole embryos, detectable from the oocyte stage but not beyond the neurula stage.[27,28] In contrast, ADRB2 RNA (*adrb2*) shows consistent expression from the oocyte to tadpole stages.[28] An RNA sequencing analysis of animal caps (an epidermal tissue explant) indicated a diminished expression of *adrb1* relative to *adrb2*.[29] The epidermal expression of *adrb2* is further supported by data from the *Xenopus* single-cell transcriptome database (https://kleintools.hms.harvard.edu). Complementing this, our *in situ* hybridization validated the presence of adrb2 in the late neurula stage epidermis (Figures S3A–S3B').

To discern whether DBT functions through ADRB in the epidermis, embryos were co-treated with the ADRB antagonist timolol (TIM), DBT, and CLA. The anticipated suppression of CLA-induced epidermal wound formation was absent when embryos were subjected to combine DBT and TIM treatment (Figures S3C–S3F). Wound ratios, determined at 10 and 60 min post-treatment, suggest that TIM antagonizes the activity of DBT (Figures S3G and S3G'). Collectively, these findings support the proposition that DBT attenuates CLA effects predominantly through ADRB2.

DBT suppresses myosin light chain phosphorylation via ADRB2 in the epidermis

To elucidate the molecular mechanism by which DBT influences CLA activity, we analyzed the distribution of phosphorylated MYL (pMyl) in epidermal cells. Under control conditions, pMyl was localized at the apical cell cortex (Figures 3A and 3G). Exposure to CLA for 10 min increased pMyl intensity at this site (Figures 3B and 3G). Treatment with DBT prior to CLA resulted in a diminished pMyl intensity (Figures 3C and 3G), suggesting that DBT potentially inhibits MYL phosphorylation. Using morpholino antisense oligonucleotides
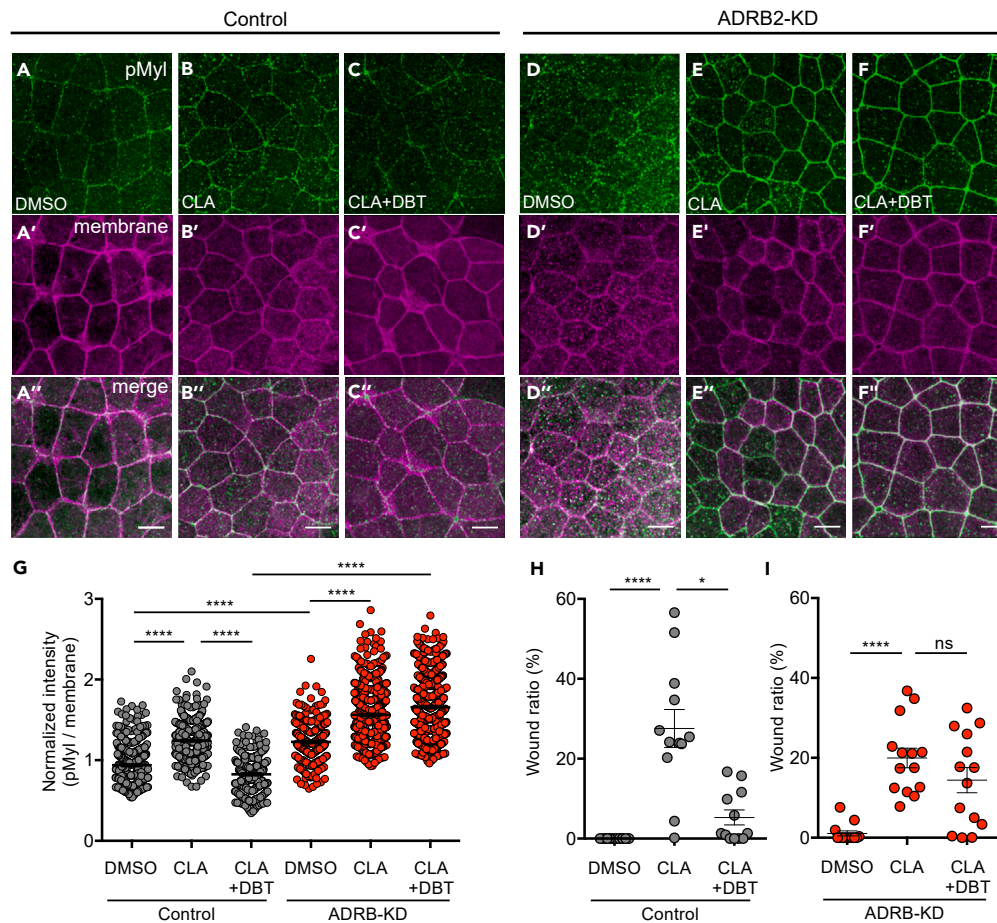
Figure 3. DBT suppresses phosphorylation of MYL by acting on ADRB2

(A–F″) Immunostaining of the epidermis using antibodies against pMyl (green), E-cad (magenta), and GFP (membrane, blue). Embryos were injected with membrane-*gfp* and control-MO (A–C) or *adrb2*-MO (40 ng/blastomere at the 4-cell stage) (D–F).

(G) Quantification of pMyl intensity at cell-cell junctions, normalized to membrane-GFP intensity (n = 316–713 cell junctions from 3 to 4 embryos, ****p < 0.0001, as assessed using one-way analysis of variance; Scale bar: 20 μm). DMSO, 250 μM; CLA, 250 nM; DBT, 1 mM. Embryos were fixed following a 10 min CLA treatment. All images are representative of 3–4 embryos in each group.

(H and I) Normalized wound ratio measurement 2 h after treatment of CLA in control (H) and *adrb2* knockdown embryos (I). (n = 12 embryos, *p = 0.0187, ****p < 0.0001, one-way analysis of variance). Data in (G), (H), and (I) are represented as mean ± SEM. (MYL, myosin light chain; pMyl, phosphorylated MYL; ADRB, beta-adrenergic receptor; E-cad, E-cadherin; MO, morpholino antisense oligonucleotides; KD, knockdown; CLA, calyculin A; DBT, dobutamine).

(MO)—a validated approach from previous study[28]—we achieved knockdown of *adrb2*. In *adrb2*-depleted embryos, DMSO and CLA treatments substantially augmented pMyl levels (Figures 3D, 3E, and 3G). In these experiments, DBT did not attenuate CLA-induced MYL phosphorylation, as evident by both the normalized intensity and raw intensity of pMyl (Figures 3F and 3G).

To further investigate the interplay between DBT and ADRB2, adrb2 knockdown embryos were co-treated with DBT and CLA. Predicated on our hypothesis that DBT would not suppress CLA-induced damage in this case, we assessed wound size 2 h post-CLA administration. The outcomes revealed that the protective effects of pre-treated DBT were less evident than in the control, with no significant difference compared to the CAL-only treatment (Figures 3H and 3I). These data collectively highlight ADRB2's role in moderating Myl phosphorylation in the epidermis and suggest that DBT acts through ADRB2.

ADRB2 is required for epidermal cell apical surface expansion and body elongation

Live-imaging was employed to elucidate the function of ADRB2 in the developing epidermis. By stage 17, the average apical surface area of control embryos was approximately 400 μm², which diminished upon *adrb2* knockdown (Figures 4A, 4B, and 4D, red bars). This reduction was restored, and even exceeded control levels, upon co-expression with an *adrb2* mRNA variant untargeted by the *adrb2* MO (5 mis-adrb2) (Figures 4C and 4D, blue bars). Such differences were also evident at stage 20 (Figures 4E–4H).

Throughout the observation period, apical surface expansion was recorded across all groups. The expansion rate, calculated from the average values among each group, showed notable differences: from 428.2 μm² to 609.9 μm² in controls, 364 μm² to 448.5 μm² in knockdown
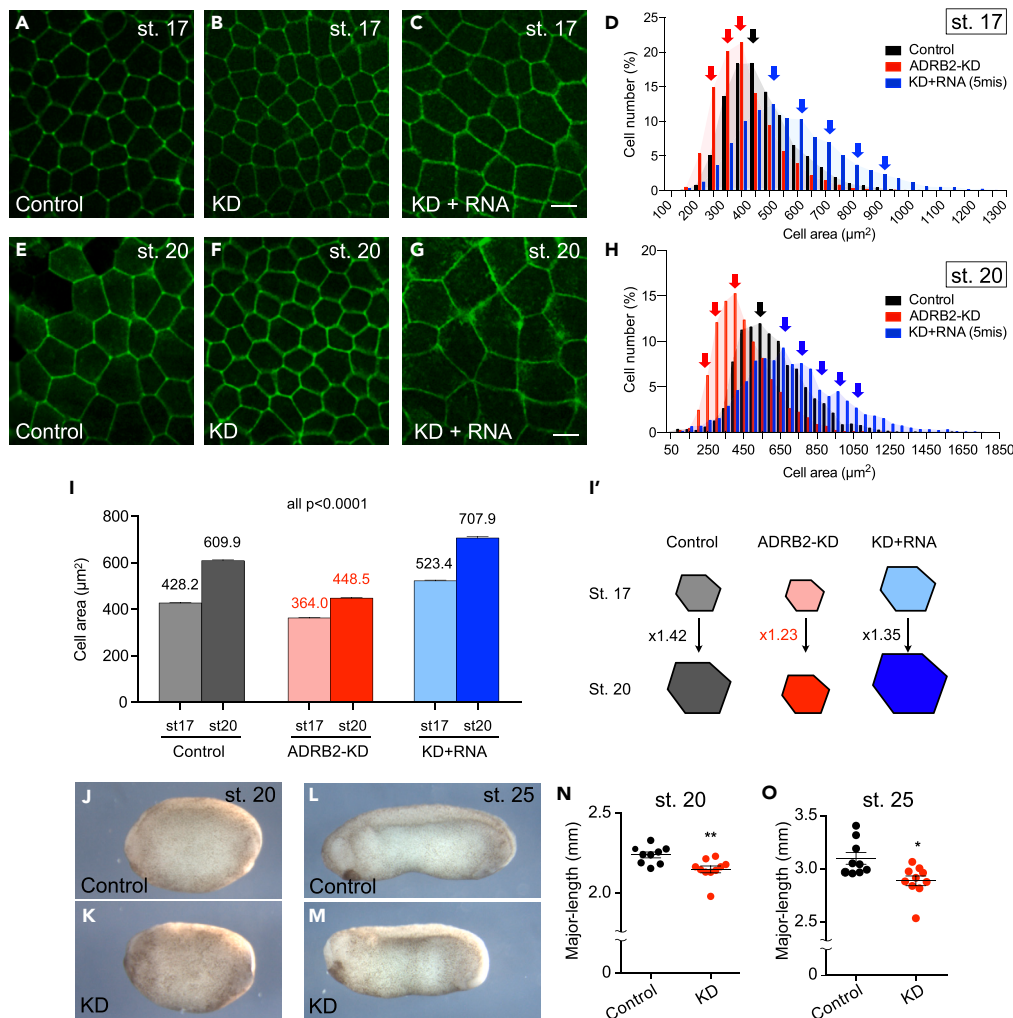
Figure 4. ADRB2 controls apical cell area

(A–C) Live-imaging of epidermis of membrane-*gfp*-injected control embryo (A), *adrb2*-KD (B), and embryos rescued by co-injection of *adrb2*-RNA (C) at stage 17.
(D) Measurement of the apical area of epidermal cells and their distribution in each group at Stage 17. (black, control; red, *adrb2*-KD; blue, rescued) (****p < 0.0001, Kolmogorov-Smirnov test. control: n = 3686 cells from 7 embryos; adrb2-KD: n = 5131 cells from 9 embryos; KD + RNA: n = 3464 cells from 10 embryos). (E–G) Live-imaging of epidermis of membrane-*gfp*-injected control embryo (E), *adrb2*-KD (F), and embryos rescued by co-injection of *adrb2*-RNA (G) at stage 20.
(H) Measurement of the apical area of epidermal cells and their distribution in each group, at Stage 20. (control: n = 2423 cells from 7 embryos, adrb2-KD: n = 4212 cells from 10 embryos, KD + RNA: n = 2594 cells from 10 embryos). (I) Comparison of the average apical cell area in each group at both stages. Numbers show the average of apical cell area.
(I') Schemes showing the fold ratio of expanded apical cell area using average from Stage 17 to Stage 20 in each group. (J–M) Images of control and KD embryos at Stage 20 (J and K) and 25 (L and M).
(N and O) Body length measurement (N, control: n = 9, KD: n = 10, **p = 0.0021; O, control: n = 9, KD: n = 10, *p = 0.01). Data in (I), (N), and (O) are represented as mean ± SEM. (GFP, green fluorescence protein; KD, knockdown).

embryos, and 523.4 μm^2 to 707.9 μm^2 in embryos co-expressing adrb2 mRNA (Figure 4I). Although the knockdown embryos exhibited a degree of expansion by stage 20, the extent of this expansion was markedly less than observed in the control embryos (Figures 4I and 4I').

Furthermore, adrb2-knockdown embryos showed several developmental aberrations. Among the most evident was a reduction in body length compared to control embryos (Figures 4J–4M). From stages 20 to 25, knockdown embryos demonstrated compromised body elongation (Figures 4N and 4O). In severe instances, epidermal peeling analogous to CLA-treated embryos was apparent. Moreover, adrb2-knockdown embryos exhibited ciliogenesis defects (Figure S4). In the *Xenopus* embryo epidermis, cilia cells emerge from deeper layers and develop multicilia.[29–31] Live-imaging during stages 25 and 30 (Figures S4A–S4F) indicated a slower expansion of the apical cell area of ciliated cells in knockdown embryos compared to controls (Figures S4G–S4H). Rescue experiments with *adrb2* RNA overexpression reinstated the typical phenotype, underscoring the pivotal role ADRB2 plays in cilia cell integration. Notably, a consistent reduction in cilia length

was observed across both stages in knockdown embryos (Figures S4A–S4F, S4I, and S4J). Notably, the restoration of cilia length by overexpressing *adrb2*-5mis RNA was not as pronounced as that of the apical cell surface area. The incomplete rescue of cilia length suggests potential unintended consequences of ADRB2 overexpression on ciliogenesis, possibly due to alterations in cortical tension. In summary, our data highlights the essential role of ADRB2 in ensuring proper apical cell surface expansion, ciliogenesis, and global body elongation.

ADRB2 regulates F-actin and myosin dynamics to ensure epidermal cell morphological stability

In the absence of ADRB2, cells displayed irregular actomyosin contraction. Normal epidermal cells maintain a stable hexagonal shape and seldom exhibit frequent contraction (Figures 5A–5B). Conversely, ADRB2-depleted cells displayed recurrent ectopic contractions across multiple adjacent cells, leading to a dynamic reduction in apical cell area within 5 min (Figures 5C and 5D; Videos S1, S2, and S3). Moreover, while the length of a single cell junction remained consistent throughout the 6 min time-lapse video in control embryos (Figures 5E and 5E'), there was noticeable sporadic contraction and relaxation of individual cell-cell junctions in the knockdown embryos (Figures 5F and 5F'; Video S4). These observations highlight the role of ADRB2 in tempering epidermal cell hypercontraction.

To delve deeper into how ADRB2 deficiency-induced hypercontraction correlates with actomyosin distribution, we visualized F-actin and myosin heavy chain using LifeAct-red fluorescence protein (RFP) and myosin intrabody SF9[32] fused with green fluorescence protein (GFP) (pCS107 as a vector), respectively (Figures 5G–5H''). We plotted the mean intensities of F-actin and myosin at cell-cell junctions to track their oscillatory behaviors (Figure S5A). Intriguingly, F-actin and myosin oscillation were asynchronous in controls but were synchronized in ADRB2-deficient cells (Figures 5I and 5J). While oscillation frequency varied between cells, distinct patterns emerged: anti-phase in controls and in-phase in knockdowns (Figures 5I', 5J', S5B, and S5C). Notably, functional actomyosin contractions that shrink cell-cell junctions showed synchronous F-actin and myosin oscillations.[14]

Given the influence of cortical actomyosin contraction on cell adhesion molecules in *Xenopus* epidermal cells,[33] we explored the impact of *adrb2* knockdown on cell adhesion. In the ADRB2 knockdown cells, the adherens junction molecules E-cadherin demonstrated decreased localization at the cell-cell border, but this reduction was not uniform (Figures S6A–S6C). Notably, certain cell-cell junctions displayed pronounced E-cadherin intensities (Figure S6B, arrows, consistent in Figure S6G), a pattern absent in control embryos (Figures S6A and S6F). The tight junction molecule ZO-1 was also reduced from the cell-cell border in knockdown embryos, though some junctions retained high intensities (Figure S6D). When comparing the ratio of E-cadherin and ZO-1, a decrease was evident in the knockdown embryos, raising the possibility that E-cadherin is more sensitive to ADRB2 knockdown. Another tight junction molecule, claudin 4, did not show marked changes by ADRB2 knockdown (Figures S6F–S6I). Yet, the staining pattern, reminiscent of the E-cadherin staining, lacked uniformity (Figures S6G and S6G' arrows and arrowheads). The intensities of E-cadherin to claudin 4 ratio in knockdown cells mirrored the E-cadherin to ZO-1 is low in the knockdown cells, same as the ratio of E-cadherin and ZO-1 intensities (Figure S6J). These observations suggest the potential regulatory role of ADRB2 in cell adhesion at the cell-cell border, with a particular emphasis on adherens junctions.

Observing the apical actomyosin mesh in the *Xenopus* epidermis enabled detailed co-localization tracking of F-actin and myosin heavy chain in control and knockdown embryos (Figures 6A–6D''). Raw intensity plot profiles of F-actin-RFP and SF9-GFP across the apical cell surface revealed an absence of co-localization in control embryos (Figure 6E). In contrast, the knockdown embryos exhibited marked co-localization between F-actin and myosin (Figure 6F, pink dotted lines). Alongside the results in Figure 5, we concluded that ADRB2 plays a role in physically and functionally dissociating F-actin from myosin at cell cortices, thereby restraining actomyosin contraction.

Ligand-binding residues are essential for ADRB2-mediated cell expansion

To discern the mode of ADRB2 action in the developing epidermis, we probed its potential interaction with ligands such as adrenaline or norepinephrine. Although the autonomic nervous system is undeveloped at the stages we examined, ADRB2 might still be activated by maternally derived ligands in the tissue.[28] We generated *adrb2* mutants lacking ligand-binding capability. Specific amino acids in murine ADRB2 are crucial for ligand interaction.[34,35] Residues Asp[113], Ser[204], and Ser[207] in ADRB2, known to bind ligands, are conserved across species as Asp[126], Ser[217], and Ser[220] in *Xenopus* (Figures 7A and 7B). We then generated two *adrb2* mutant constructs that exhibited compromised ligand-binding due to these amino acid substitutions.

Overexpression of wild-type *adrb2* led to an increase in the apical cell area (Figures 7C and 7D). However, a single mutation, Asp[126] to glycine (G), resulted in only a minimal effect (Figures 7C, 7E, and 7G). More prominently, substitutions at Ser[217] and Ser[220] to alanine (A) further diminished the apical surface expansion (Figures 7F–7H). These results suggest that ADRB2 regulates the apical cell area hinges on ligands such as adrenaline and norepinephrine, even in the absence of a mature nervous system.

DISCUSSION

In this study, we conducted chemical screening on *Xenopus* embryos to elucidate the molecular underpinnings governing the morphological flexibility of developing epithelial tissues. Our results identified ADRB as a key regulator of actomyosin contractility in the embryonic epidermis during stages preceding the complete maturation of the adrenergic nervous system. ADRB2 emerged as pivotal in suppressing excessive actomyosin contractions, ensuring both maintenance and adaptive expansion of the apical surface of epidermal cells. Moreover, our data emphasize the importance of ADRB2 ligand binding for its optimal function in epidermal contexts. Collectively, our study highlights the significance of ADRB2 in regulating tissue extensibility and safeguarding the structural integrity of the developing epithelium.
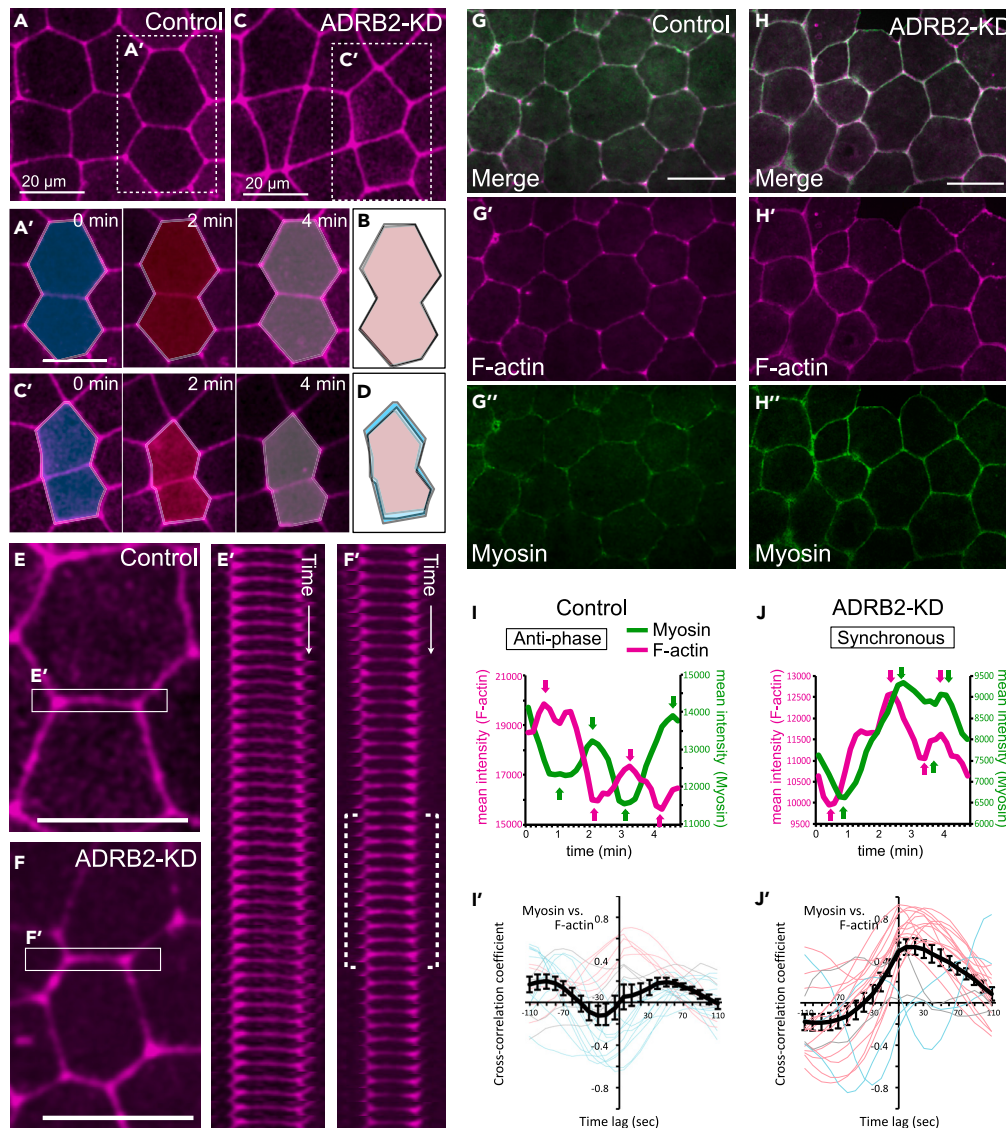
Figure 5. ADRB2 silences actomyosin contraction by unlinking F-actin and myosin

(A–D) Live-imaging of epidermis injected with LifeAct-*rfp* in control (A) and *adrb2*-knockdown embryos (C). (A') and (C') are still images taken every 2 min from time-lapse videos of control and knockdown embryos, respectively.

(B and D) Diagrams overlaying the outlines of two cells at three different time points of (A') and (C'), with each outline shown in distinct colors. Scale bar: 20 μm. All presented images are representative samples from more than 10 embryos imaged in each group.

(E–F') Representative images and kymographs of individual epidermal cell junctions in control (E and E') and knockdown embryos (F and F'). The dotted bracket in the F' kymograph indicates a period where the cell junction temporarily contracts.

(G–H'') Live-imaging of the epidermis injected with both LifeAct-*rfp* and SF9-*gpf*. (G–G')': control embryos; (H–H''): knockdown embryos.

(I and J) The mean intensities of LifeAct-RFP and SF9-GFP were measured over time (I: control, J: knockdown).

(I'–J') Cross-correlation of raw intensities of SF9 and LifeAct along cell junctions in control (I) and knockdown embryos (J'). Each red and blue line represents the result from individual cell junctions. The red line indicates synchronous oscillation, and the blue line indicates anti-phase oscillation.

Understanding regulators like ADRB in epidermal morphogenesis provides insights into how epithelial cells coordinate their morphology to maintain tissue coherence. While actomyosin contractility directs cellular movements and embryonic tissue reshaping,[36,37] molecules enhancing this contractility are central to several developmental pathways.[14] The roles of ADRB2 in actomyosin relaxation and modulating cell adhesion are important to counterbalance these contractions. This facilitates the epithelium in maintaining its structural integrity and supports the expansion of its apical surfaces. Such a buffering mechanism against mechanical distortion could be beneficial in sequential developmental processes, notably ciliogenesis and body elongation. This intricate equilibrium underscores the value of regulatory elements in preserving the morphology and deformability of epithelial tissues.
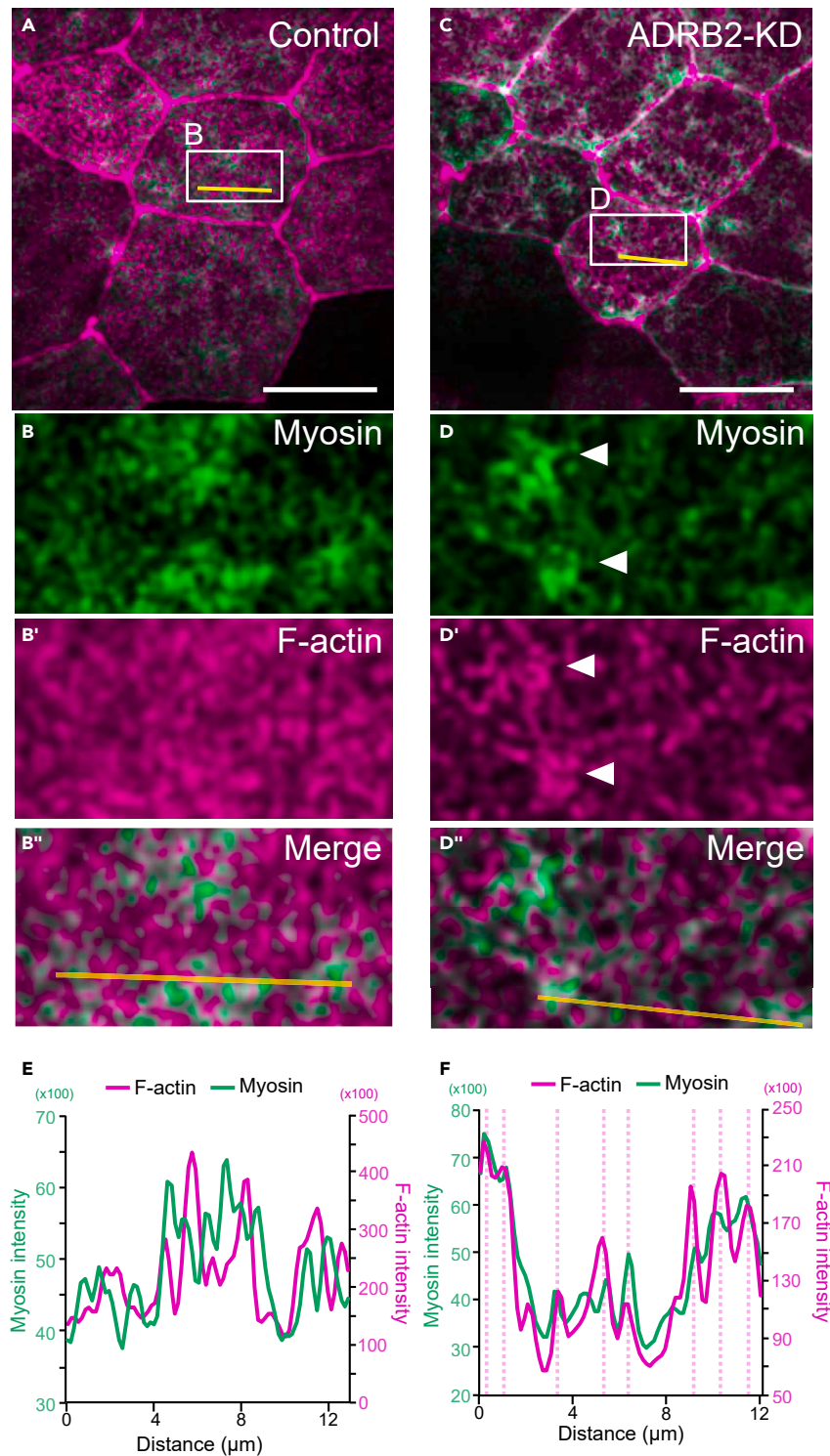
Figure 6. ADRB2 facilitates actomyosin complex on the apical surface of the epidermis

(A–D″) Live imaging of the apical surface of the epidermis injected with LifeAct-*rfp* and SF9-*gpf*. (A–B′)': control embryos; (C–D′)': knockdown embryos. Arrowheads indicate excess myosin accumulation in the knockdown embryos. Scale bar: 20 µm.

(E and F) Plot profile of raw intensities for LifeAct-RFP and SF9-GFP along the drawn line (yellow) in images (B″) and (D″), respectively. The pink dotted lines in F indicate overlapping peaks between LifeAct-RFP and SR9-GFP.
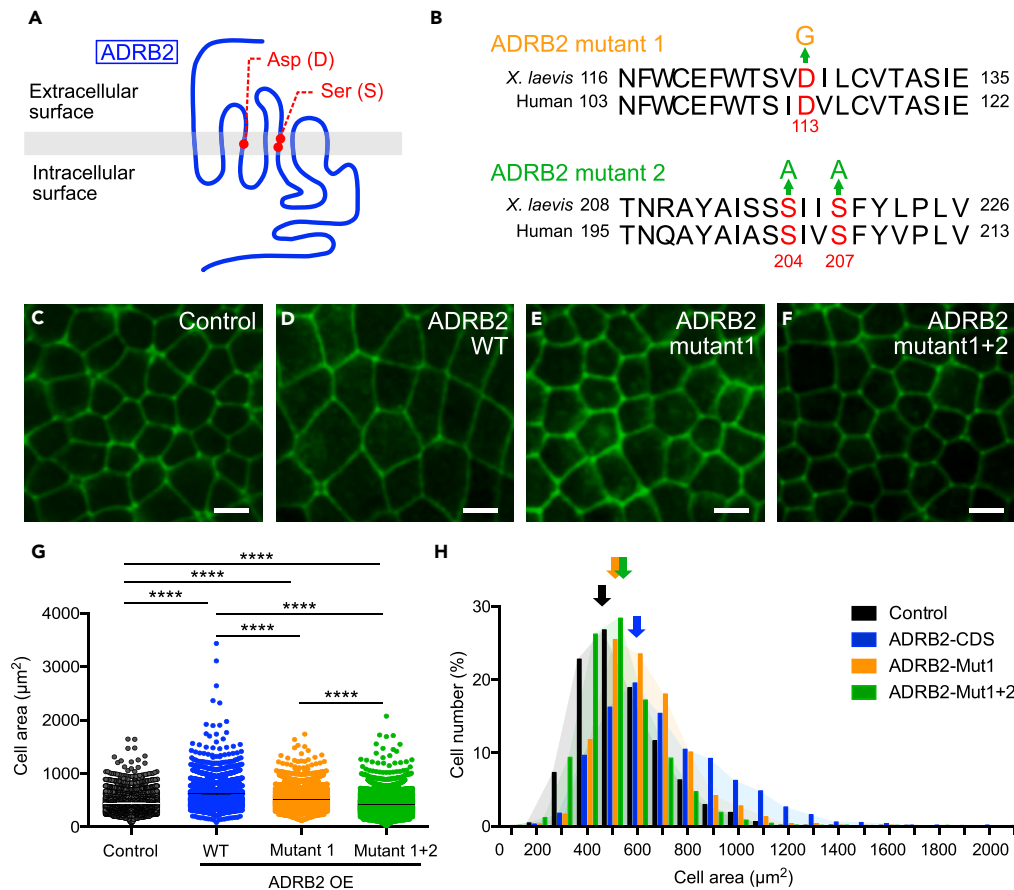
Figure 7. ADRB2 requires ligands to expand apical cell area

(A) Prototypic model of ADRB2. Red circles indicate residues involved in ligand binding (Asp: aspartic acid, Ser: serine).

(B) Mutant ADRB2s used in the experiments. Upper is mutant 1, where Asp has been replaced by Gly. Lower is mutant 2, where Ser has been replaced by Ala. These mutations are established in human ADRB2.

(C–F) Live imaging of the membrane-GFP expressing epidermis of control (only endogenous ADRB2), co-expressing WT ADRB2 (300 pg), mutant 1 ADRB2 (300 pg), and mutant 2 ADRB2 (300 pg).

(G) Quantification and (H) distribution of apical cell area in each group. Arrows indicate the peak of each group. ADRB, beta-adrenergic receptor; WT, wild-type (control: n = 3851 cells from 8 embryos, WT adrb2: n = 2099 cells from 6 embryos, mutant 1: n = 3873 cells from 8 embryos, mutant 2: n = 5533 cells from 8 embryos, ****p < 0.0001, as assessed using one-way analysis of variance) Data in H are represented as mean $\pm$ SEM. Scale bar: 20 μm.

Considering the established role of ADRB in adult human organs, our identification of this receptor as a regulator of actomyosin dynamics in the embryonic epidermis aligns with existing literature. Notably, our screening identified opposing roles for ADRB and ADRA in the epidermal context. This dichotomy mirrors their known roles in mature smooth muscles,[18,38–40] suggesting conserved receptor-mediated mechanisms governing tissue dynamics, irrespective of direct regulation by adrenergic nerves.[26,41]

One of the central discoveries of our research is the ligand-dependent role of ADRB in determining the extensibility of the epithelium. This finding offers insights into the physiology of mature epithelial organs influenced by the adrenergic autonomic nervous system. The potential roles of ADRB2 in the tracheal epithelium underscore the importance of this receptor in regulating cell morphology.[42–44] While the role of ADRB2 in the cilia beating of tracheal epithelial cells is known,[45] its impact on tracheal cell morphology remains elusive. Given the similarities between the Xenopus epidermis and mammalian trachea,[29,46,47] ADRB2 in the tracheal epithelium might adjust the apical cell surface in sync with noradrenaline-driven tracheal muscle expansion. Drawing from our results, we posit an expanded role for epithelial ADRB2, which could synergize with the action of smooth muscles in mature organs.

Future investigations should focus on elucidating the sources of ADRB2 ligands and their downstream effectors in the embryonic epidermis. Our evidence points to potential intracellular sources of ligands, but the exact mechanisms of engagement with receptors remain to be determined. Furthermore, understanding how ADRB2 signaling disrupts actomyosin filament functionality, a known determinant of actomyosin contractility, is essential.[48,49] In airway smooth muscle, ADRB stimulation has been shown to elevate cyclic adenosine monophosphate, activating protein kinase A. This kinase phosphorylates various targets, such as MLCK, culminating in muscle relaxation.[50–52] Investigating potential conserved mechanisms involving cyclic adenosine monophosphate, protein kinase A, and MLCK will be essential for future research.

In conclusion, our study demonstrates the molecular mechanisms governing epithelial cell shape stability and tissue extensibility during development. The findings reveal the role of ADRB2 in regulating actomyosin dynamics, possibly counterbalancing mechanical strains during embryonic body elongation. The potential conservation of these mechanisms in mature adrenergic organs might offer a blueprint for understanding epithelial deformability in diverse physiological homeostasis.

Limitations of the study

While our chemical assay identified ADRB2 as a regulator of actomyosin relaxation, its role as the primary effector is yet to be conclusively determined. Other critical regulators might have remained undetected in our chemical screening, potentially due to the compounds not exhibiting their effects at the concentrations we used. Our data highlight the criticality of ligand binding by demonstrating a mutated ADRB2 that lacks this ability. However, the molecular and cellular mechanisms governing ligand supply, including the triggers for ligand-receptor binding, have not been thoroughly elucidated in our study. Furthermore, the causal relationship between actomyosin relaxation and the function of cell adhesion cannot be determined from our current experiments, warranting further investigation.

STAR★METHODS

Detailed methods are provided in the online version of this paper and include the following:

- KEY RESOURCES TABLE
- RESOURCE AVAILABILITY
  - Lead contact
  - Materials availability
  - Data and code availability
- EXPERIMENTAL MODEL AND STUDY PARTICIPANT DETAILS
  - *X. laevis* embryo preparation and microinjection
- METHOD DETAILS
  - Chemical screening
  - Chemicals
  - Whole-mount *in situ* hybridization
  - mRNA for live-imaging and MOs
  - ADRB2 constructs
  - Immunostaining and antibodies
  - Embryo imaging using confocal microscopy
- QUANTIFICATION AND STATISTICAL ANALYSIS

SUPPLEMENTAL INFORMATION

Supplemental information can be found online at https://doi.org/10.1016/j.isci.2023.108469.

AUTHOR CONTRIBUTIONS

Conceptualization, A. Shindo; Methodology, Y. M., N. K., A. Sato, and A. Shindo; Investigation, Y. M., K. N., and A. Shindo; Project administration, A. Shindo; Writing, A. Shindo; Supervision, A. Shindo.

DECLARATION OF INTERESTS

The authors declare no competing or financial interests.

INCLUSION AND DIVERSITY

We support inclusive, diverse, and equitable conduct of research.

REFERENCES

1. Poznanski, A., Minsuk, S., Stathopoulos, D., and Keller, R. (1997). Epithelial cell wedging and neural trough formation are induced planarly in Xenopus, without persistent vertical interactions with mesoderm. Dev. Biol. *189*, 256–269.

2. Keller, R., and Sutherland, A. (2020). Convergent extension in the amphibian, Xenopus laevis. Curr. Top. Dev. Biol. *136*, 271–317.

3. Bertet, C., Sulak, L., and Lecuit, T. (2004). Myosin-dependent junction remodelling controls planar cell intercalation and axis elongation. Nature *429*, 667–671.

4. Blankenship, J.T., Backovic, S.T., Sanny, J.S.P., Weitz, O., and Zallen, J.A. (2006). Multicellular rosette formation links planar cell polarity to tissue morphogenesis. Dev. Cell *11*, 459–470.

5. Lee, C., Scherr, H.M., and Wallingford, J.B. (2007). Shroom family proteins regulate gamma-tubulin distribution and microtubule architecture during epithelial cell shape change. Development *134*, 1431–1441.

6. Morita, H., Kajiura-Kobayashi, H., Takagi, C., Yamamoto, T.S., Nonaka, S., and Ueno, N. (2012). Cell movements of the deep layer of non-neural ectoderm underlie complete neural tube closure in Xenopus. Development *139*, 1417–1426.

7. Fernandez-Gonzalez, R., and Peifer, M. (2022). Powering morphogenesis: Multiscale challenges at the interface of cell adhesion and the cytoskeleton. Mol. Biol. Cell *33*. pe4–10.

8. Agarwal, P., and Zaidel-Bar, R. (2019). Principles of actomyosin regulation in vivo. Trends Cell Biol. *29*, 150–163.

9. Miao, H., and Blankenship, J.T. (2020). The pulse of morphogenesis: Actomyosin dynamics and regulation in epithelia. Development *147*, dev186502.

10. Hirano, K., Derkach, D.N., Hirano, M., Nishimura, J., and Kanaide, H. (2003). Protein kinase network in the regulation of phosphorylation and dephosphorylation of smooth muscle myosin light chain. Mol. Cell. Biochem. *248*, 105–114.

11. Ikebe, M., and Hartshorne, D.J. (1985). Phosphorylation of smooth muscle myosin at two distinct sites by myosin light chain kinase. J. Biol. Chem. *260*, 10027–10031.

12. Amano, M., Ito, M., Kimura, K., Fukata, Y., Chihara, K., Nakano, T., Matsuura, Y., and Kaibuchi, K. (1996). Phosphorylation and activation of myosin by Rho-associated kinase (Rho-kinase). J. Biol. Chem. *271*, 20246–20249.

13. Levayer, R., and Lecuit, T. (2013). Oscillation and polarity of E-cadherin asymmetries control actomyosin flow patterns during morphogenesis. Dev. Cell *26*, 162–175.

14. Shindo, A., Inoue, Y., Kinoshita, M., and Wallingford, J.B. (2019). PCP-dependent transcellular regulation of actomyosin oscillation facilitates convergent extension of vertebrate tissue. Dev. Biol. *446*, 159–167.

15. Kaneko-Kawano, T., Takasu, F., Naoki, H., Sakumura, Y., Ishii, S., Ueba, T., Eiyama, A., Okada, A., Kawano, Y., and Suzuki, K. (2012). Dynamic regulation of myosin light chain phosphorylation by Rho-kinase. PLoS One *7*, e39269.

16. Peterson, L.J., Rajfur, Z., Maddox, A.S., Freel, C.D., Chen, Y., Edlund, M., Otey, C., and Burridge, K. (2004). Simultaneous stretching and contraction of stress fibers in vivo. Mol. Biol. Cell *15*, 3497–3508.

17. Herbomel, G., Hatte, G., Roul, J., Padilla-Parra, S., Tassan, J.P., and Tramier, M. (2017). Actomyosin-generated tension on cadherin is similar between dividing and non-dividing epithelial cells in early Xenopus laevis embryos. Sci. Rep. *7*, 45058.

18. Dror, R.O., Arlow, D.H., Maragakis, P., Mildorf, T.J., Pan, A.C., Xu, H., Borhani, D.W., and Shaw, D.E. (2011). Activation mechanism of the β2-adrenergic receptor. Proc. Natl. Acad. Sci. USA *108*, 18684–18689.

19. de Lucia, C., Eguchi, A., and Koch, W.J. (2018). New insights in cardiac β-adrenergic signaling during heart failure and aging. Front. Pharmacol. *9*, 904.

20. Kato, S., and Inomata, H. (2023). Blastopore gating mechanism to regulate extracellular fluid excretion. iScience *26*, 106585.

21. Li, J., Zhang, S., Soto, X., Woolner, S., and Amaya, E. (2013). ERK and phosphoinositide 3-kinase temporally coordinate different modes of actin-based motility during embryonic wound healing. J. Cell Sci. *126*, 5005–5017.

22. Robie, N.W., Nutter, D.O., Moody, C., and McNay, J.L. (1974). In vivo analysis of adrenergic receptor activity of dobutamine. Circ. Res. *34*, 663–671.

23. Ruffolo, R.R., Spradlin, T.A., Pollock, G.D., Waddell, J.E., and Murphy, P.J. (1981). Alpha and beta adrenergic effects of the stereoisomers of dobutamine. J. Pharmacol. Exp. Ther. *219*, 447–452.

24. Rasmussen, H., Kelley, G., and Douglas, J.S. (1990). Interactions between Ca^{2+} and cAMP messenger system in regulation of airway smooth muscle contraction. Am. J. Physiol. *258*, L279–L288.

25. Piascik, M.T., and Perez, D.M. (2001). α1-Adrenergic receptors: New insights and directions. J. Pharmacol. Exp. Ther. *298*, 403–410.

26. Tanaka, Y., Horinouchi, T., and Koike, K. (2005). New insights into β-adrenoceptors in smooth muscle: Distribution of receptor subtypes and molecular mechanisms triggering muscle relaxation. Clin. Exp. Pharmacol. Physiol. *32*, 503–514.

27. Devic, E., Paquereau, L., Steinberg, R., Caput, D., and Audigier, Y. (1997). Early expression of a β1-adrenergic receptor and catecholamines in Xenopus oocytes and embryos. FEBS Lett. *417*, 184–190.

28. Mori, S., Moriyama, Y., Yoshikawa, K., Furukawa, T., and Kuroda, H. (2013). β-Adrenergic signaling promotes posteriorization in Xenopus early development. Dev. Growth Differ. *55*, 350–358.

29. Chung, M.I., Kwon, T., Tu, F., Brooks, E.R., Gupta, R., Meyer, M., Baker, J.C., Marcotte, E.M., and Wallingford, J.B. (2014). Coordinated genomic control of ciliogenesis and cell movement by RFX2. Elife *3*, e01439.

30. Sedzinski, J., Hannezo, E., Tu, F., Biro, M., and Wallingford, J.B. (2016). Emergence of an apical epithelial cell surface in vivo. Dev. Cell *36*, 24–35.

31. Ventura, G., Amiri, A., Thiagarajan, R., Tolonen, M., Doostmohammadi, A., and Sedzinski, J. (2022). Multiciliated cells use filopodia to probe tissue mechanics during epithelial integration in vivo. Nat. Commun. *13*, 6423.

32. Hashimoto, H., Robin, F.B., Sherrard, K.M., and Munro, E.M. (2015). Sequential contraction and exchange of apical junctions drives zippering and neural tube closure in a simple chordate. Dev. Cell *32*, 241–255.

33. Stephenson, R.E., Higashi, T., Erofeev, I.S., Arnold, T.R., Leda, M., Goryachev, A.B., and Miller, A.L. (2019). Rho flares repair local tight junction leaks. Dev. Cell *48*, 445–459.e5.

34. Strader, C.D., Candelore, M.R., Hill, W.S., Dixon, R.A., and Sigal, I.S. (1989). A single amino acid substitution in the β-adrenergic receptor promotes partial agonist activity from antagonists. J. Biol. Chem. *264*, 16470–16477.

35. Strosberg, A.D. (1993). Structure, function, and regulation of adrenergic receptors. Protein Sci. *2*, 1198–1209.

36. Shindo, A., and Wallingford, J.B. (2014). PCP and septins compartmentalize cortical actomyosin to direct collective cell movement. Science *343*, 649–652.

37. Dehapiot, B., Clément, R., Alégot, H., Gazsó-Gerhát, G., Philippe, J.M., and Lecuit, T. (2020). Assembly of a persistent apical actin network by the formin Frl/Fmnl tunes epithelial cell deformability. Nat. Cell Biol. *22*, 791–802.

38. Giembycz, M.A., and Newton, R. (2006). Beyond the dogma: Novel β2-adrenoceptor signalling in the airways. Eur. Respir. J. *27*, 1286–1306.

39. Miller, J.R., Silver, P.J., and Stull, J.T. (1983). The role of myosin light chain kinase phosphorylation in beta-adrenergic

relaxation of tracheal smooth muscle. Mol. Pharmacol. *24*, 235–242.

40. Obara, K., and de Lanerolle, P. (1989). Isoproterenol attenuates myosin phosphorylation and contraction of tracheal muscle. J. Appl. Physiol. (1985) *66*, 2017–2022.

41. Rajashree, R., Blunt, B.C., and Hofmann, P.A. (2005). Modulation of myosin phosphatase targeting subunit and protein phosphatase 1 in the heart. Am. J. Physiol. Heart Circ. Physiol. *289*, H1736–H1743.

42. Salathe, M. (2002). Effects of β-agonists on airway epithelial cells. J. Allergy Clin. Immunol. *110*, S275–S281.

43. Nguyen, L.P., Al-Sawalha, N.A., Parra, S., Pokkunuri, I., Omoluabi, O., Okulate, A.A., Windham Li, E., Hazen, M., Gonzalez-Granado, J.M., Daly, C.J., et al. (2017). β2-adrenoceptor signaling in airway epithelial cells promotes eosinophilic inflammation, mucous metaplasia, and airway contractility. Proc. Natl. Acad. Sci. USA *114*, E9163–E9171.

44. Davis, P.B., Silski, C.L., Kercsmar, C.M., and Infeld, M. (1990). β-Adrenergic receptors on human tracheal epithelial cells in primary culture. Am. J. Physiol. *258*, C71–C76.

45. Yanaura, S., Imamura, N., and Misawa, M. (1981). Effects of β-adrenoceptor stimulants on the canine tracheal ciliated cells. Jpn. J. Pharmacol. *31*, 951–956.

46. Walentek, P., and Quigley, I.K. (2017). What we can learn from a tadpole about ciliopathies and airway diseases: Using systems biology in Xenopus to study cilia and mucociliary epithelia. Genesis *55*.

47. Walentek, P. (2021). Xenopus epidermal and endodermal epithelia as models for mucociliary epithelial evolution, disease, and metaplasia. Genesis *59*, e23406.

48. Verkhovsky, A.B., Svitkina, T.M., and Borisy, G.G. (1995). Myosin II filament assemblies in the active lamella of fibroblasts: Their morphogenesis and role in the formation of actin filament bundles. J. Cell Biol. *131*, 989–1002.

49. Ebrahim, S., Chen, D., Weiss, M., Malec, L., Ng, Y., Rebustini, I., Krystofiak, E., Hu, L., Liu, J., Masedunskas, A., et al. (2019). Dynamic polyhedral actomyosin lattices remodel micron-scale curved membranes during exocytosis in live mice. Nat. Cell Biol. *21*, 933–939.

50. Freyer, A.M., Billington, C.K., Penn, R.B., and Hall, I.P. (2004). Extracellular matrix modulates β2-adrenergic receptor signaling in human airway smooth muscle cells. Am. J. Respir. Cell Mol. Biol. *31*, 440–445.

51. Morgan, S.J., Deshpande, D.A., Tiegs, B.C., Misior, A.M., Yan, H., Hershfeld, A.V., Rich, T.C., Panettieri, R.A., An, S.S., and Penn, R.B. (2014). β-agonist-mediated relaxation of airway smooth muscle is protein kinase A-dependent. J. Biol. Chem. *289*, 23065–23074.

52. Ouedraogo, N., and Etienne, R. (2014). Physiology of airway smooth muscle contraction: An overview. J. Pulm. Respir. Med. *04*, 1000221.

53. Shindo, A., Audrey, A., Takagishi, M., Takahashi, M., Wallingford, J.B., and Kinoshita, M. (2018). Septin-dependent remodeling of cortical microtubule drives cell reshaping during epithelial wound healing. J. Cell Sci. *131*, jcs212647.

54. Sive, H.L., Grainger, R.M., and Harland, R.M. (2000). Early Development of Xenopus laevis: A Laboratory Manual (Cold Spring Harb Lab Press).

55. Nandadasa, S., Tao, Q., Menon, N.R., Heasman, J., and Wylie, C. (2009). N- and E-cadherins in Xenopus are specifically required in the neural and non-neural ectoderm, respectively, for F-actin assembly and morphogenetic movements. Development *136*, 1327–1338.

STAR★METHODS

KEY RESOURCES TABLE

REAGENT or RESOURCE	SOURCE	IDENTIFIER
Antibodies		
Chicken anti-GFP	Abcam	Cat # ab13970; RRID: AB_300798
Mouse anti-E-cadherin	BD Biosciences	Cat # 610181; RRID: AB_397580
Rabbit anti-ZO-1	Thermo Fisher Scientific	Cat # 61-7300; RRID: AB_138452
Rabbit anti-Claudin 4	Invitrogen	Cat # 36-4800; RRID: AB_2533262
Rabbit anti-phospho myosin light chain	CST	Cat # 3671; RRID: AB_330248
Alexa-Fluor 488 goat anti-rabbit IgG (H + L)	Thermo Fisher Scientific	Cat # A-11008; RRID: AB_143165
Alexa-Fluor 555 goat anti-mouse IgG (H + L)	Thermo Fisher Scientific	Cat # A-21422; RRID: AB_2535844
Alexa-Fluor 405 goat anti-chicken IgY (H + L)	Abcam	Cat # ab175674; RRID: AB_2890171
Chemicals, peptides, and recombinant proteins		
Calyculin A	Wako Pure Chemical Corporation	Cat # 032-14451
Dobutamine	Tokyo Chemical Industry	Cat # D4335
Y27632	Enzo Life Science	Cat # ALX-271-333-M005
Blebbistatin	Wako Pure Chemical Corporation	Cat # 027-17043
Isoproterenol	Tokyo Chemical Industry	Cat # I0260
Salbutamol	Tokyo Chemical Industry	Cat # S0531
Timolol	Wako Pure Chemical Corporation	Cat # 206-19491
SCH772984	MedChemExpress	Cat # HY-50846
GSK690693	MedChemExpress	Cat # HY-10249
Critical commercial assays		
HiFi DNA Assembly	New England Biolabs	Cat # E2621
MMESSAGE mMACHINE SP6 Transcription Kit	Thermo Fisher Scientific	Cat # AM1340
Experimental models: Organisms/strains		
Wild type Xenopus laevis frogs	Watababe zoushoku	N/A
Oligonucleotides		
Primer: adrb2.L, forward: 5′-cgacaggccaatctggccgcgcatggaacggtcggtcag -3′	This paper, order from IDT	N/A
Primer: adrb2.L, reverse: 5′-cttagatatcggccggccgcctataataagcaatcatgcgt gttatgattttg -3′	This paper, order from IDT	N/A
Primer: 5mis adrb2, forward: 5′-agaggctcgagaggccttgcctataataagcaatcatgcgtgttatg -3′	This paper, order from IDT	N/A
Primer: 5mis adrb2, reverse: 5′-agaggctcgagaggccttgcctataataagcaatcatgcgtgttatg -3′	This paper, order from IDT	N/A
Primer: adrb2 fragment1-common, forward: 5′-cgacaggccaatctggccgcatggaacggtcggtcagc -3′	This paper, order from IDT	N/A
Primer: adrb2 fragment1-common, reverse: 5′-tgacgcaaaggattcccaccgaggtccag -3′	This paper, order from IDT	N/A
Primer: adrb2 fragment2- mutant1, forward: 5′-catctccttctacttgcctctggtggtc -3′	This paper, order from IDT	N/A

(Continued on next page)

Continued

REAGENT or RESOURCE	SOURCE	IDENTIFIER
Primer: adrb2 fragment2- mutant2, forward: 5′-ggtgggaatcctttgcgtcactgccagcatcgagacc -3′	This paper, order from IDT	N/A
Primer: adrb2 fragment2-common, reverse: 5′-gaggcaagtagaaggagatgatggaagaggag -3′	This paper, order from IDT	N/A
Primer: adrb2 fragment2-mutant2: reverse: 5′-gaggcaagtagaatgcgatgattgcagaggagatggcataagcac -3′	This paper, order from IDT	N/A
Primer: adrb2 fragment3-mutant1: forward: 5′-catctccttctacttgcctctggtggtc -3′	This paper, order from IDT	N/A
Primer: adrb2 fragment3-mutant2: forward: 5′-catcgcattctacttgcctctggtggtc -3′	This paper, order from IDT	N/A
Primer: adrb2 fragment3-common: reverse: 5′-agaggctcgagaggccttgcctataataagcaatcatgcgtgttatg -3′	This paper, order from IDT	N/A
Software and algorithms		
FIJI v1.52p	ImageJ	https://fiji.sc/ RRID: SCR_002285
GraphPad Prism 6.0/10.0	GraphPad Software	https://www.graphpad.com/scientific-software/prism/ RRID: SCR_002798

RESOURCE AVAILABILITY

Lead contact

Further information and requests for resources and reagents should be directed to and will be fulfilled by the lead contact, Asako Shindo (shindo@kumamoto-u.ac.jp).

Materials availability

- This study did not generate new unique reagents.

Data and code availability

- This paper does not have new datasets.
- This paper does not report original code.
- Any additional information required to reanalyze the data reported in this paper is available from the lead contact upon request.

EXPERIMENTAL MODEL AND STUDY PARTICIPANT DETAILS

X. laevis embryo preparation and microinjection

The procedure for obtaining embryos from adult female frogs has been described previously.[53] Briefly, female frogs were injected with human chorionic gonadotropin and incubated overnight at 16°C. The eggs were fertilized *in vitro*, dejelled in a 3% (w/v) cysteine solution at the 2-cell stage, and then reared in 1/3× Marc's Ringer's (MR) solution (https://wiki.xenbase.org/xenwiki/index.php/Culture_media). The embryos were microinjected at the 4-cell stage with 3% (w/v) Ficoll® in 1/3× MR solution and reared in 3% (w/v) Ficoll® solution.

METHOD DETAILS

Chemical screening

For this study, 152 compounds were randomly selected from the FDA-approved drug library available at the ITbM Chemical Library Center of Nagoya University (Aichi, Japan). For the experiment, 5–10 embryos were treated with each compound (10 μM) and CLA (250 nM and 500 nM) in a 2-mL total volume with 1/3× MR solution (Figure 2). One and two hours after the treatment, images of the embryos were acquired using a stereomicroscope (SMZ800N, Nikon, Japan), and the wound and embryo surface areas were measured using ImageJ (https://imagej.nih.gov/ij/). A heat-map based on wound ratio was generated using WebMeV (http://mev.tm4.org/).

Chemicals

The following commercial compounds were used for sequential experiments: Calyculin A (032–14451, Wako Pure Chemical Corporation, Japan), Y27632 (ALX-271-333-M005, Enzo Life Science, USA), Blebbistatin (027–17043, Wako Pure Chemical Corporation), Dobutamine

(D4335, Tokyo Chemical Industry, Japan), isoproterenol (I0260, Tokyo Chemical Industry), salbutamol (S0531, Tokyo Chemical Indusry), Timolol (206–19491, Wako Pure Chemical Corporation), SCH772984 (HY-50846, MedChemExpress, USA), and GSK690693 (HY-10249, MedChemExpress, USA). In the experiments conducted following the chemical screening, we used a commercial dobutmine at concentrations ranging from 250 μM to 1mM. Note that dobutamine should be administered prior to CLA treatment to achieve its effects efficiently.

Whole-mount *in situ* hybridization

In situ hybridization was performed as previously described.[54] Briefly, the viteline membrane of embryos was removed using forceps, and the embryos were fixed using MEMFA (1:1:8 solution of 10✕ minimum essential medium salts, formaldehyde, and RNase-free H_2O), for 2 h at room temperature. The fixed RNAs are hybridized with a digoxigenin-labeled probe. After the hybridization step, the digoxigenin was detected with alkaline-phosphatase-linked antibodies. The ADRB2 probe was designed and synthesized for full-length *adrb2.L*. The *adrb2.L* sequence was inserted into the pCS10R vector using HiFi DNA Assembly (E2621, New England Biolabs, USA). The primers used for *adrb2.L* cloning were: cgacaggccaatctggccgcatggaacggtcggtcagc and agaggctcgagaggccttgcctataataagcaatcatgcgtgttatgattttttg.

mRNA for live-imaging and MOs

Capped mRNA was synthesized using the mMESSAGE mMACHINE™ SP6 Transcription kit (AM1340, Thermo Fisher Scientific, USA). The following amounts of mRNAs were injected into the ventral blastomere, at the 4-cell stage, to target the epidermis: 60 pg membrane-*gfp*, 40 pg LifeAct-*rfp*, and 20 pg sf9-*gfp*. MOs, including Standard Control oligo (5′-CCTCTTACCTCAGTTACAATTTATA-3′), were purchased from Gene Tools (https://www.gene-tools.com/). The *adrb2* MO (5′-GGCTGGCGCTGACCGACCGTTCCAT-3′) has been described previously,[28] and 40 ng of it was injected per ventral blastomere, at the 4-cell stage. The 5mis adrb2 (5′-atggagcggtctgttagcgctagtccgaat-3′) rescue construct was designed as previously published.[28]

ADRB2 constructs

HiFi DNA Assembly was used to construct adrb2-related plasmids (in the vector pCS10R). The primers used were as follows: WT adrb2: Fw: cgacaggccaatctggccgcgcatggaacggtcggtcag, Rev: cttagatatcggccggccgcctataataagcaatcatgcgtgttatgattttttg; 5mis adrb2: Fw: cgacaggccaatctggccgcatggagcggtctgttagcgctagtcc, Rev: agaggctcgagaggccttgcctataataagcaatcatgcgtgttatg. To construct mutant ADRB2 by means of HiFi DNA Assembly, the adrb2 whole sequence was divided into three fragments. The primers were designed as follows: Fragment 1 common Fw: cgacaggccaatctggccgcatggaacggtcggtcagc; Fragment 1 common Rev: tgacgcaaaggattcccaccgaggtccag; Fragment 2 for mutant 1 Fw: catctccttctacttgcctctggtggtc; Fragment 2 for mutant 2 Fw: ggtgggaatcctttgcgtcactgccagcatcgagacc; Fragment 2 common Rev: gaggcaagtagaaggagatgatggaagaggag; Fragment 2 for mutant 2 Rev: gaggcaagtagaatgcgatgattgcagaggagatggcataagcac; Fragment 3 for mutant 1 Fw: catctccttctacttgcctctggtggtc; Fragment 3 for mutant 2 Fw: catcgcattctacttgcctctggtggtc; Fragment 3 common Rev: agaggctcgagaggccttgcctataataagcaatcatgcgtgttatg. The three fragments were assembled and inserted into the pCS10R vector.

Immunostaining and antibodies

The vitelline membrane of the injected embryos was removed using forceps and the embryos were fixed using 2% trichloroacetic acid (TCA), and immunostaining was performed as described previously.[53,55] Briefly, the embryos were incubated in 2% TCA for 25 minutes at 25°C, following by washing with 0.3% Triton x100/PBS (PBST). After overnight incubation with the primary antibody at 4°C, the samples were rinsed with PBST and then treated with the secondary antibody for 2h at 25°C. Following this, the samples were washed with PBST. The following primary antibodies were used: chicken anti-GFP (1:500; ab13970, Abcam, UK), mouse anti-E-cadherin (1:300; 610181, BD Biosciences, USA), rabbit anti-ZO-1 (1:300; 61-7300, Thermo Fishers, USA), rabbit anti-claudin 4 (1:200; 36-4800, Invitrogen, USA), rabbit anti-pMyl (1:200; 3671, CST). The following secondary antibodies were used: Alexa Fluor® 488 goat anti-rabbit IgG (H+L) (1:300; A-11008, Thermo Fisher Scientific, USA), Alexa Fluor® 555 goat anti-mouse IgG (H+L) (1:300; A-21422, Thermo Fisher Scientific, USA), and Alexa Fluor® 405 goat anti-chicken IgY (H+L) (1:1000; ab175674, Abcam, UK).

Embryo imaging using confocal microscopy

For live-imaging, the vitelline membrane of the injected embryos was removed using forceps, after the blastopore had completely closed. Embryos were reared in 1/3✕ MR solution until Stage 17. Each embryo was mounted in a glass-bottom dish containing 1/3✕ MR solution using the Yokogawa CellVoyager™ CV1000 Confocal Scanner Box (Yokogawa Electric, Japan) and Evident IXplore Spin (only for Figure S6). The time-lapse videos were taken every 10 sec, for 6–7 min.

For imaging of immunostained embryos, the embryos were dehydrated with methanol after staining. The embryos were cleared using a 2:1 solution of benzyl benzoate and benzoic acid, and then imaged using the confocal microscopy.

QUANTIFICATION AND STATISTICAL ANALYSIS

Statistical analyses were performed using Prism version 6 and 10, GraphPad Software Inc. Statistical tests for each analysis are described in the figure legends.